Journal of Materials Chemistry A

Antisolvent processing of lead halide perovskite thin films studied by in-situ X-ray diffraction

Journal:	*Journal of Materials Chemistry A*
Manuscript ID	TA-COM-06-2018-006025.R1
Article Type:	Communication
Date Submitted by the Author:	06-Sep-2018
Complete List of Authors:	Brüning, Karsten; SLAC National Accelerator Laboratory, Materials Science Division Tassone, Christopher; Stanford Synchrotron Radiation Lightsource, Materials Science

Antisolvent processing of lead halide perovskite thin films studied by in-situ X-ray diffraction

Karsten Bruening[*,1], Christopher J. Tassone[*,1]

[1] SSRL Materials Science Division, SLAC National Accelerator Laboratory, Menlo Park, California 94025, United States

[*]Corresponding Authors:

*Email: tassone@slac.stanford.edu, bruening@slac.stanford.edu

Phone.: +1 650 926 3124

Keywords: Hybrid organic – inorganic perovskite photovoltaics, *in situ* X-ray diffraction, blade coating, solvent exchange, antisolvent

Abstract

The conversion mechanism from the precursor ink to the perovskite film using antisolvent-induced crystallization has been studied using in-situ X-ray diffraction during blade coating and antisolvent deposition. We study various solvent systems forming methylammonium lead iodide perovskite. We find that it is critical to add the antisolvent before the formation of a crystalline intermediate phase. Compared to thermal crystallization, the antisolvent-induced crystallization alters the conversion route. Instead of heterogeneous nucleation and conversion through a crystalline intermediate phase, antisolvent-assisted annealing leads to a rapid direct crystallization, resulting in highly regular smooth films.

Introduction

Lead halide perovskite photovoltaics have seen an enormous rise in research interest and in power conversion efficiencies over the last seven years. Their attractiveness lies in their solution processability combined with excellent photovoltaic performance. Most commonly, thin films are cast from a precursor solution, which is then converted into the photo-active perovskite phase. In order to achieve this, most recipes include a thermal annealing step to promote the crystallization of perovskite. In addition to the thermal annealing, a significant percentage of high-efficiency devices were obtained using protocols that involve a solvent exchange process (fig. S1). An antisolvent, with solubility properties orthogonal to the precursor solvent, is added to the wet film, which leads to a rapid supersaturation of the precursor solution and consequently to a rapid precipitation of crystalline perovskite. The films made using this so-called "antisolvent method" exhibit a morphology distinct from purely thermally annealed samples and typically show better device performance.[1–3] Antisolvent annealing has been used in combination with spin coating as well as blade coating.[4] It is commonly observed that the timing of antisolvent deposition is critical.[2,4]

However, despite the popularity of this method, the fundamental differences in the conversion and crystallization mechanisms compared to purely thermal annealing remain unclear. We performed antisolvent annealing on blade-coated films in situ with synchrotron X-ray diffraction to analyze the evolution of the precursor phase, perovskite phase and film thickness as a function of antisolvent deposition time and annealing temperature. A better understanding of the fundamental processes governing the antisolvent-assisted conversion will facilitate the design of recipes that enable robust antisolvent annealing. Moreover, knowledge gained about why antisolvent-induced crystallization typically yields superior films could be applied to antisolvent-free crystallization routes. For instance, recently rapid thermal crystallization has been shown to

give films of similar performance as antisolvent-annealed films, with the perovskite crystallization occurring on similarly short time scales.[5–7]

It has been widely reported that most perovskite crystallization routes go through intermediate phases.[1,5,8–23] For the classic recipe containing methylammonium iodide (MAI) and lead(II)iodide (PbI_2) in dimethylformamide (DMF), UV-vis absorption studies indicate the presence of iodoplumbate Lewis adducts, with each Pb^{2+} cation coordinated with up to nine solvent molecules, yielding species such as $[PbI_3S_3]^-$ (S = solvent).[24–26] Depending on the solvent system, the solvent molecules compete with the iodide to make up the coordination sphere. The more Lewis-basic the solvent is (the higher the tendency to donate an electron pair), the more likely it is to replace an iodide anion. The donor number D_N has been found to correlate with the coordination between Pb^{2+} and the solvent.[27,28] Upon supersaturation due to solvent evaporation, the coordination complexes arrange into an intermediate crystalline lattice, not unlike that of PbI_2, with solvent molecules and potentially MAI intercalated between layers of PbI_2. This structure templates the perovskite structure. Thermal annealing finally extracts the intercalated solvent molecules and leads to the formation of the desired perovskite phase. Conventional slow thermal annealing (e.g. 20 min at 100°C) however leads to an undesired morphology consisting of polycrystalline needles, resulting from heterogeneous nucleation and potentially from preferred growth facets and low-angle grain boundaries within needles.

On the contrary, crystallization driven by antisolvent addition has been shown to yield homogeneous smooth films. The antisolvent has to be chosen such that it has good solubility for the original solvent, but poor solubility for the precursor salts, forcing the precursor to precipitate. The precipitation occurs either in the form of perovskite or in the form of an

intermediate which subsequently is transformed into perovskite.[1,29,30] Various solvents have been screened as antisolvents, e.g. chlorobenzene, toluene, diethylether.[2,9]

In this study, we use chlorobenzene, one of the most popular antisolvents. We perform in situ XRD during antisolvent annealing of blade-coated films to elucidate the conversion mechanisms of thermal annealing and of antisolvent annealing.[31]

In an inert helium atmosphere, precursor ink is deposited onto a glass substrate and is spread out into a film using a blade coater (figs. 1a, S2). Following the deposition, antisolvent is added at different times through a spray nozzle such that the film is completely covered in less than a second. Immediately after covering the film with chlorobenzene, the film is blown dry using pressurized helium. Finally, the film is thermally annealed at 100°C for 20 min (including ramp-up time). X-ray diffraction measurements with an incident angle of 2.5° and a time resolution of up to 50 ms are taken during the entire process. The thickness is monitored using interferometry (see SI) and the film color is recorded with a video camera.

The precursor ink has the composition 1:1 MAI:PbI_2 with 30 mol% (excess, relative to MAI) of MACl additive at a total concentration of 45 wt.%.[4] Following established recipes, we used three solvent systems: a) DMF, b) DMSO:DMF 9:8 and c) NMP:DMF 9:8. The solvent systems will be referred to as 'DMF', 'DMSO' and 'NMP' from now on.

First, we observe the drying of the blade-coated films and their transformation to the crystalline intermediate phase without addition of antisolvent at room temperature (figs. 1 b-d, S3-S5). The as-coated films are amorphous with thicknesses ranging from 4 to 9 µm, depending on the viscosity of the solvent. In all films, a diffuse low-angle scattering ($0.4 < q \cdot Å < 0.7$) is present from the beginning, which turns into distinct diffraction peaks once the film reaches a thickness within 30 to 40 % of its final thickness. The transformation to the crystalline intermediate species

is accompanied by an increase in opacity and a change in color with a slight shift to the red. The transition occurs after 20 s, 5 min, 6 min in DMF, NMP, DMSO, respectively.

For the three solvent systems, three distinct crystalline intermediate species form, evidenced by distinct X-ray diffractograms (fig. 2a). For NMP and DMSO, the precursor salts preferentially coordinate with these solvent molecules rather than with DMF due to the lower donor number of DMF.[28] The observed species agree well with previous reports. In the case of DMF[17] and DMSO [15,21], the intermediate species contains MAI and solvent molecules intercalated between layers of PbI_2, whereas the NMP intermediate does not contain MAI. While the DMF and DMSO intermediates are stable at room temperature, the NMP intermediate undergoes another phase transition into the perovskite phase, starting at 10 to 15 min (fig. 1c). We note that the thickness measured by interferometry is about 1.5 to 4 µm, which we ascribe to the presence of solvent-rich amorphous phases. The final thickness of all films after thermal annealing was about 1 µm. We hypothesize that the onset time and rate of the formation of the crystalline intermediate are governed by the supersaturation, which in turn depends on the initial film thickness (viscosity), solubility and vapor pressure.[4] The nature of the crystalline species depends on the solvent-salt interaction, as quantified by Gutmann's donor number.[24,27,28]

Next, we performed thermal annealing of blade-coated films at 100°C for 20 min (incl. heating from room temperature). The heating step began as soon as the coating was finished. As expected, the films go through the same crystalline intermediate phase as in the simple drying scenario. The formation of the crystalline intermediate phase is accelerated at higher temperatures due to the increased solvent evaporation rate (fig. 2, S6-S17). The formation of perovskite is complete from a crystallographic perspective after 2 to 10 min. As expected, the morphology of those films is very rough, containing pillars (NMP), needles (DMF) or large

flower-like domains (DMSO). As mentioned above, the purpose of antisolvent annealing is to avoid the formation of these morphologies in favor of a smooth film of relatively small grains. In the next step, we explore how the addition of antisolvent at various drip times changes the conversion mechanisms. Across all solvent systems, we found that the properly timed addition of chlorobenzene leads to a rapid direct crystallization of perovskite without evidence for crystalline intermediates. This transition only occurs completely if the chlorobenzene is added before the crystalline intermediate phase is formed (fig. 3a). If chlorobenzene is added during partial conversion to the crystalline intermediate, we hypothesize that only the unconverted part can be directly converted to perovskite, while the remaining crystalline intermediate can only be thermally converted (e.g. DMF, 2 min, fig. 2b), as thermal energy is required to release the intercalated solvent from the crystalline intermediate. In the extreme case of adding chlorobenzene after the formation of the crystalline intermediate is completed, it has very little effect (NMP 20min, fig. 2c). On the other hand, if antisolvent addition occurs prematurely, there is still too much solvent to achieve rapid oversaturation and only little perovskite is formed directly. However, even though the majority of perovskite is formed thermally, the morphology is dominated by the antisolvent-induced crystallization, which possibly templates the thermal crystallization. The morphologies of the films after the thermal annealing step are shown in figs. 2 and S18. These findings are in line with a recent study by Li et al., investigating chlorobenzene antisolvent addition in a MAI/PbI_2 in DMSO:GBL system using in-situ spin coating, reporting that direct conversion from the amorphous sol-gel phase to the perovskite phase occurs if the antisolvent is added 10 s before formation of a crystalline intermediate.[0864][32]

We find that the optimum time for antisolvent dripping is bound by solvent evaporation towards short times and by crystalline intermediate formation towards long times. In-between these

137 bounds, perovskite formation after antisolvent deposition occurs directly without crystalline
138 intermediate (at least not detectable by XRD). We hypothesize that the smooth films are created
139 by a homogeneous nucleation with a high nucleation density, compared to heterogeneous
140 nucleation with a low nucleation density under purely thermal annealing. The observed change in
141 color and opacity of the film agrees well with the in-situ XRD data about the formation of the
142 crystalline intermediate. For that reason, the color and opacity can serve as an indicator to guide
143 the timing of the antisolvent deposition in practice. We note that despite vastly different
144 morphologies and conversion pathways, the final film is always perovskite, as evidenced by
145 XRD and UV-vis spectroscopy (figs. S19, S20).
146 In conclusion, this study provided insight into the underlying mechanisms that govern the timing
147 of antisolvent annealing of perovskite thin films (fig. 3b). In situ XRD during antisolvent
148 annealing revealed that the antisolvent has to be added before the formation of the crystalline
149 intermediate in order to enable a direct crystallization of perovskite following a homogeneous
150 nucleation, bypassing the crystalline intermediate, which leads to unfavorable morphologies.
151

152 **Methods**

153 **Solution preparation:** MAI (Dyesol) and PbI_2 in a molar ratio of 1:1 were dissolved in either
154 DMF or DMSO:DMF 9:8 (v:v) or NMP:DMF 9:8 (v:v) at a concentration of 1.25 mol/l.[4] 30
155 mol% MACl (relative to MAI) was added. All chemicals were supplied by Sigma and used as
156 received unless noted otherwise.

157 **Substrate preparation:** Microscope glass slides (Fisher Scientific) 75x25x1 mm^3 were used as
158 substrates. All substrates were sonicated in Hellmanex solution, water, acetone and isopropanol
159 for 15 min each, blow dried and treated by UV-ozone for 20 min.

160 **Blade coating:** Films were blade-coated on a custom-made blade coater using a glass blade, a
161 blade gap of 120 µm, a blade speed of 5 mm/s in helium atmosphere (relative humidity < 1 %).
162 About 25 µl solution was used per film. About 2 ml of chlorobenzene were added quickly using
163 a remote controlled syringe pump. Directly after completion of the antisolvent deposition, the
164 film was blow-dried using a helium nozzle operated at a flow rate of 100 cm^3/s for 5 s.

165 ***In situ* XRD:** The blade coater was mounted on beamline 7-2 at the Stanford Synchrotron
166 Radiation Lightsource (SSRL). The X-ray energy was set to 12.5 keV. The incident angle was
167 2.5°. A Dectris Pilatus 300K detector was used at a distance of roughly 200 mm. In order to
168 minimize beam damage, XRD images were acquired at a framerate of 10 Hz for 15 s, followed
169 by 0.03 to 0.1 Hz for the remaining time (0.1 s exposure time). The X-ray impinged on the
170 middle of the substrate. To check for beam damage, which would show as sample heterogeneity,
171 the beam was scanned across the sample after the in-situ experiment.

172 The data was analyzed using self-written routines based on the pyFAI and pygix modules[33,34].
173 The relative phase fractions were obtained from the most prominent diffraction peak of the
174 corresponding species.

175 **Film characterization:** SEM was done on a FEI Sirion at 5 keV in SE mode using an ET or
176 TTL detector. UV-vis spectroscopy was done on a Varian Cary UV-vis spectrophotometer. Film
177 thickness measurements were made using a Thetametrisis FR-pOrtable interferometer.

178 **Acknowledgements**

179 The work at the Stanford Synchrotron Radiation Lightsource was funded by the Department of
180 Energy under Contract No. DE-AC02-76SF00515. Stanford Synchrotron Radiation Lightsource
181 at the SLAC National Accelerator Laboratory is a national user facility operated by Stanford

University on behalf of the US Department of Energy, Office of Basic Energy Sciences. Part of this work was performed at the Stanford Nano Shared Facilities (SNSF), supported by the National Science Foundation under award ECCS-1542152. K.B. thanks Dean Skoien and Valery Borzenets (SSRL) for support with the blade coater and Bart Johnson (SSRL) for beamline support.

Author Contributions

K.B. and C.J.T. conceived of and designed the experiments. K.B. carried out the in situ experiments, analyzed the WAXD data, performed film characterization measurements and designed the in-situ blade coating device. All authors contributed to writing the manuscript.

Conflicts of Interest

There are no conflicts to declare.

References

1 N. J. Jeon, J. H. Noh, Y. C. Kim, W. S. Yang, S. Ryu and S. Il Seok, *Nat. Mater.*, 2014, **13**, 897–903.

2 M. Xiao, F. Huang, W. Huang, Y. Dkhissi, Y. Zhu, J. Etheridge, A. Gray-Weale, U. Bach, Y. B. Cheng and L. Spiccia, *Angew. Chemie - Int. Ed.*, 2014, **53**, 9898–9903.

3 A. J. Pearson, *J. Mater. Res.*, 2017, **32**, 1798–1824.

4 M. Yang, Z. Li, M. O. Reese, O. G. Reid, D. H. Kim, S. Siol, T. R. Stockert, Y. Yan, J. J. Berry, M. F. A. M. Van Hest and K. Zhu, *Nat. Energy*, 2017, **2**, 17038.

5 Y. Zhong, R. Munir, J. Li, M.-C. Tang, M. R. Niazi, K. Zhao and A. Amassian, *ACS Energy Lett.*, 2018, **3**, 1078–1085.

6 S. Sanchez, X. Hua, N. Phung, U. Steiner and A. Abate, *Adv. Energy Mater.*, 2018, **1702915**, 1–7.

7 C. Chang, Y. Huang, C. Tsao and W. Su, *ACS Appl. Mater. Interfaces*, 2016, **8**, 26712–26721.

8 A. Wakamiya, M. Endo, T. Sasamori, N. Tokitoh, Y. Ogomi, S. Hayase and Y. Murata, *Chem. Lett.*, 2014, **43**, 711–713.

9 N. Ahn, D.-Y. Son, I.-H. Jang, S. M. Kang, M. Choi and N.-G. Park, *J. Am. Chem. Soc.*, 2015, **137**, 8696–8699.

10 X. Guo, C. McCleese, C. Kolodziej, A. C. S. Samia, Y. Zhao and C. Burda, *Dalt. Trans.*, 2016, **45**, 3806–3813.

11 I. Wharf, T. Gramstad, R. Makhija and M. Onyszchuk, *Can. J. Chem.*, 1976, **54**, 3430–3438.

12 D. Nenon, J. A. Christians, L. M. Wheeler, J. Blackburn, E. M. Sanehira, B. Dou, K. Zhu, J. J. Berry and J. M. Luther, *Energy Environ. Sci.*, 2016, **9**, 2072–2082.

13 R. Munir, A. D. Sheikh, M. Abdelsamie, H. Hu, L. Yu, K. Zhao, T. Kim, O. El Tall, R. Li, D. Smilgies and A. Amassian, *Adv. Mater.*, 2017, **29**, 1604113.

14 F. Hao, C. C. Stoumpos, Z. Liu, R. P. H. Chang and M. G. Kanatzidis, *J. Am. Chem. Soc.*, 2014, **136**, 16411.

15 H. Tanaka and E. Nakamura, *J. Am. Chem. Soc.*, 2015, **137**, 15907–15914.

16 B. Dou, V. L. Pool, M. F. Toney and F. A. M. Van Hest, *Chem. Mater.*, 2017, **29**, 5931–5941.

17 A. A. Petrov, I. P. Sokolova, N. A. Belich, G. S. Peters, P. V Dorovatovskii, Y. V Zubavichus, V. N. Khrustalev, V. Petrov, M. Grätzel, E. A. Goodilin and A. B. Tarasov, *J. Phys. Chem. C*, 2017, **121**, 20739–20743.

18 F. Liu, E. Schaible, A. Hexemer, C. Wang, Y. Liu, W. Zhang and M. Gra, *Nat. Commun.*, 2017, **8**, 15688.

19 Y. Jo, K. S. Oh, M. Kim, K. H. Kim, H. Lee, C. W. Lee and D. S. Kim, *Adv. Mater. Interfaces*, 2016, **3**, 1–7.

20 H. Miyamae, Y. Numahata and M. Nagata, *Chem. Lett.*, 1980, 663–664.

21 Y. Rong, Z. Tang, Y. Zhao, X. Zhong, S. Venkatesan, H. Graham, M. Patton, Y. Jing, A. M. Guloy and Y. Yao, *Nanoscale*, 2015, **7**, 10595–10599.

22 D. Shen, X. Yu, X. Cai, M. Peng, Y. Ma, X. Su, L. Xiao and D. Zou, *J. Mater. Chem. A*, 2014, **2**, 20454–20461.

23 R. Kang, J. Yeo, H. Jun, S. Lee, M. Kang, N. Myoung, S. Yim, S. Oh and D. Kim, *Nano Energy*, 2016, **27**, 175–184.

24 S. Rahimnejad, A. Kovalenko, S. M. Forés, C. Aranda and A. Guerrero, *ChemPhysChem*, 2016, 2795–2798.

25 J. Stevenson, B. Sorenson, V. H. Subramaniam, J. Raiford, P. P. Khlyabich, Y. L. Loo and P. Clancy, *Chem. Mater.*, 2017, **29**, 2435–2444.

26 K. Yan, M. Long, T. Zhang, Z. Wei, H. Chen, S. Yang and J. Xu, *J. Am. Chem. Soc.*, 2015, **137**, 4460–4468.

27 X. B. Cao, C. L. Li, L. L. Zhi, Y. H. Li, X. Cui, Y. W. Yao, L. J. Ci and J. Q. Wei, *J. Mater. Chem. A*, 2017, **5**, 8416–8422.

28 J. C. Hamill, J. Schwartz and Y.-L. Loo, *ACS Energy Lett.*, 2018, **3**, 92.

29 N. Sakai, S. Pathak, H.-W. Chen, A. a. Haghighirad, S. D. Stranks, T. Miyasaka and H. J. Snaith, *J. Mater. Chem. A*, 2016, **4**, 4464–4471.

30 J. W. Jung, S. T. Williams and A. K.-Y. Jen, *RSC Adv.*, 2014, **4**, 62971–62977.

31 J. Schlipf and P. Müller-Buschbaum, *Adv. Energy Mater.*, 2017, **7**, 1700131.

32 J. Li, R. Munir, Y. Fan, K. Zhao, J. Li, R. Munir, Y. Fan, T. Niu, Y. Liu, Y. Zhong and Z. Yang, *Joule*, 2018, **2**, 1313–1330.

33 T. G. Dane, pygix, https://github.com/tgdane/pygix, (accessed 8 December 2017).

34 G. Ashiotis, A. Deschildre, Z. Nawaz and J. P. Wright, *J. Appl. Crystallogr.*, 2015, **48**, 510–519.

Figures:

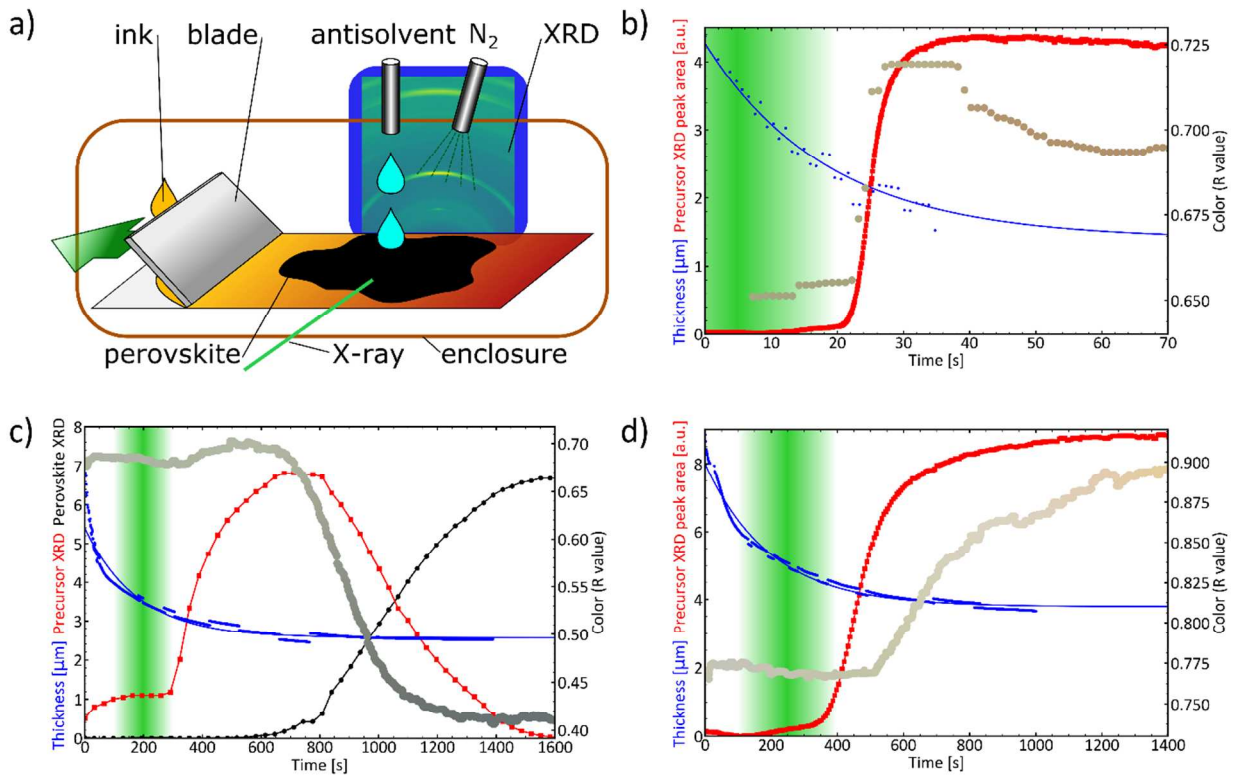

Figure 1 | Experimental setup and observation of phase transitions of blade coated films during drying. (a) Schematic of blade coating setup with in situ X-ray diffraction. (b-c) [(b) DMF, (c) NMP, (d) DMSO] Evolution of film thickness (blue dots), integrated crystalline intermediate XRD signal (a.u., red squares), integrated perovskite XRD signal (a.u., black circles), film color (red channel on ordinate, curve plotted in actual film color) over time (after blade coating) during drying at room temperature. The time window for optimum antisolvent deposition is indicated in green.

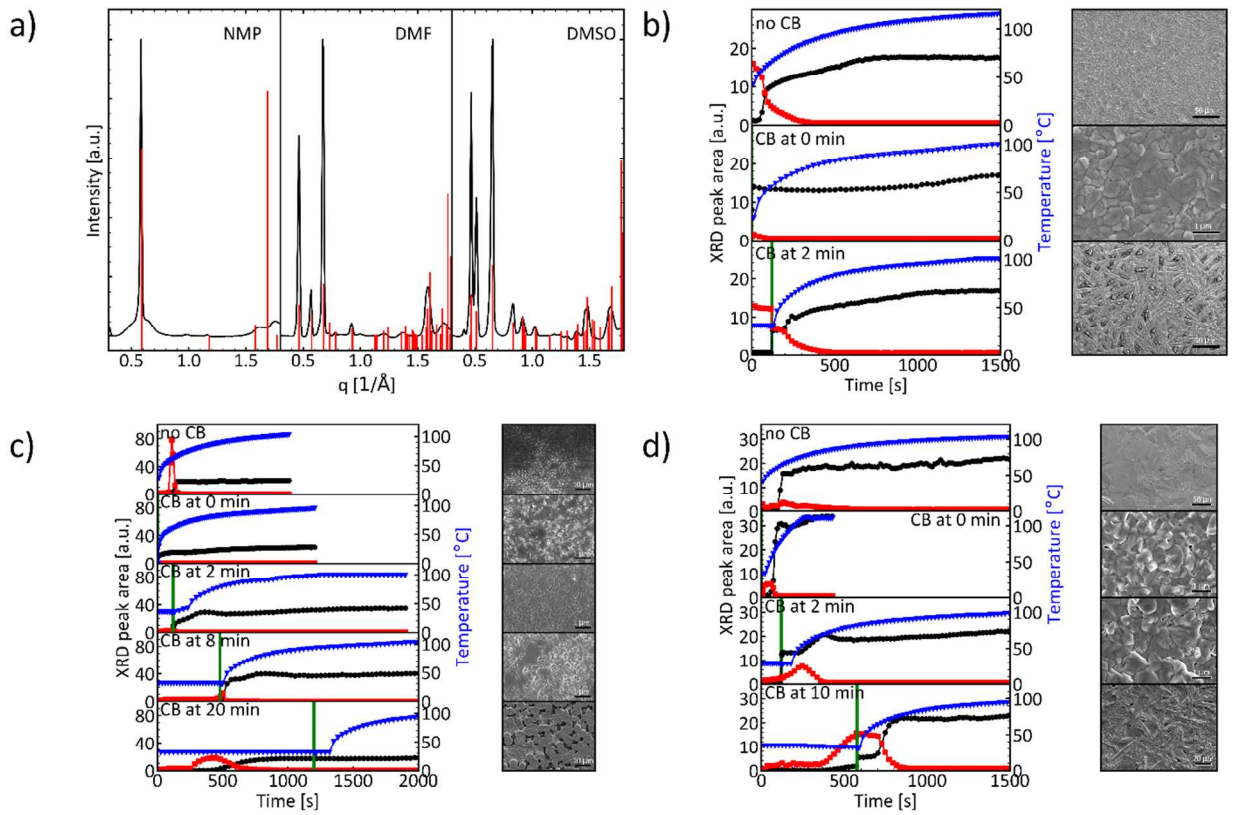

Figure 2 | Structure and morphology evolution for various antisolvent deposition times. (a) XRD of crystalline intermediates (measured: black, calculated: red), (b-d) [(b) DMF, (c) NMP, (d) DMSO] Left: integrated XRD signal (red squares: intermediate, black circles: perovskite) and temperature (blue triangles) over time (after blade coating). The vertical green bar represents the time at which chlorobenzene is added. Right: SEM images of the corresponding finished films. See fig. S18 for enlarged SEM images.

a)

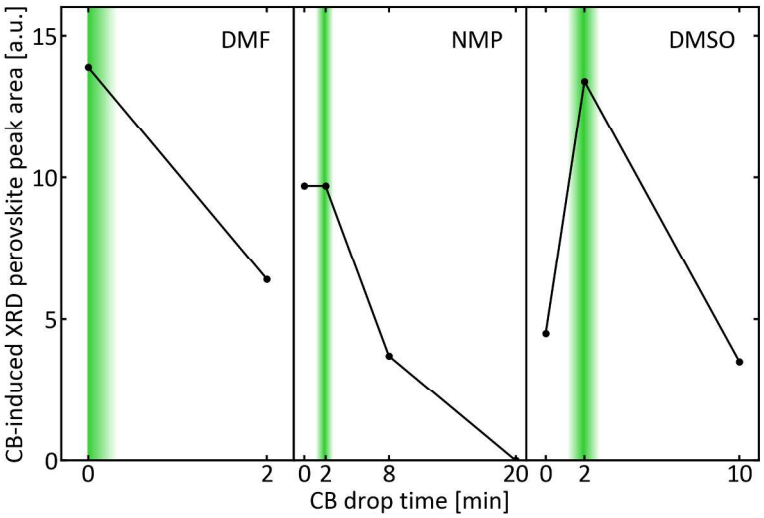
CB-induced XRD perovskite peak area [a.u.]
15
10
5
0
DMF
NMP
DMSO
0
2
0 2
8
20
0 2
10
CB drop time [min]

b)

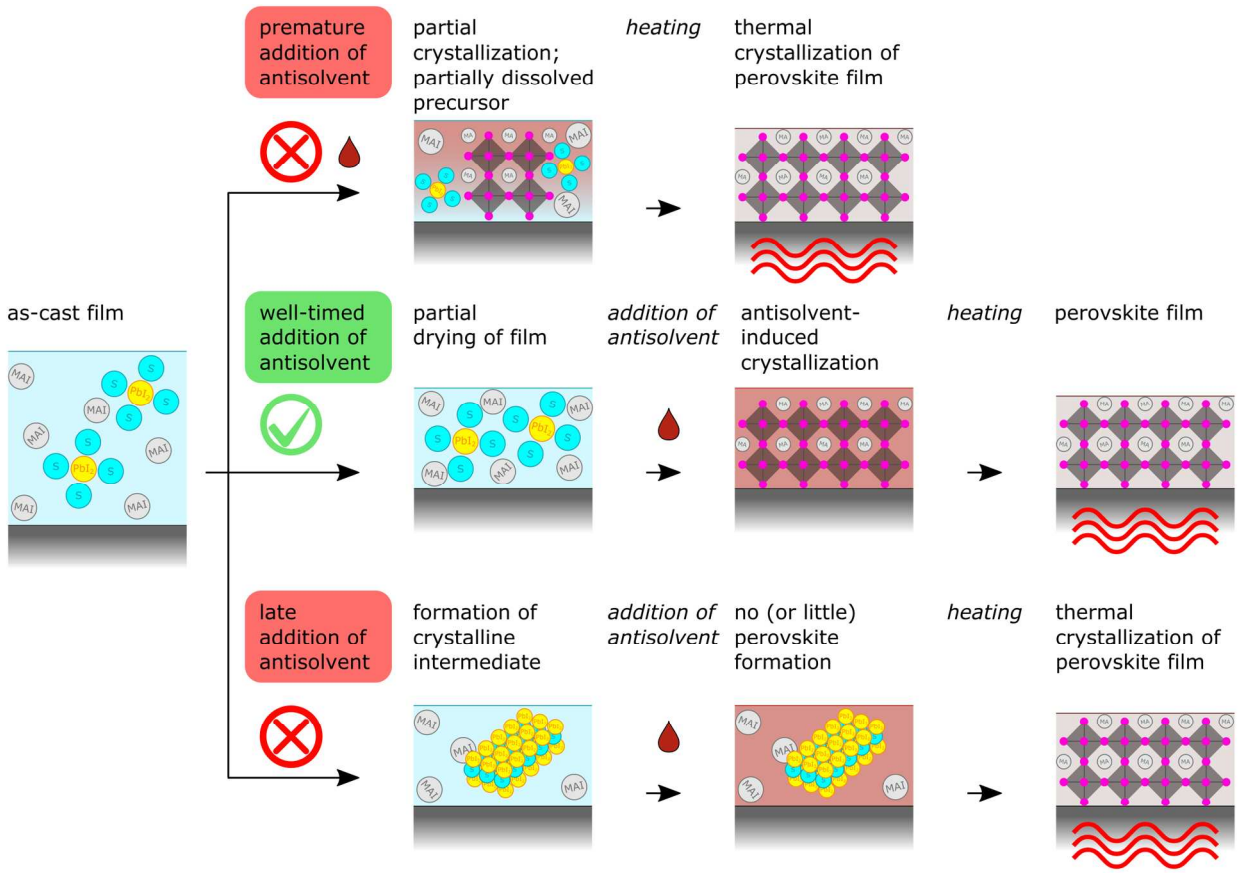
premature addition of antisolvent
partial crystallization; partially dissolved precursor
heating
thermal crystallization of perovskite film
as-cast film
well-timed addition of antisolvent
partial drying of film
addition of antisolvent
antisolvent-induced crystallization
heating
perovskite film
late addition of antisolvent
formation of crystalline intermediate
addition of antisolvent
no (or little) perovskite formation
heating
thermal crystallization of perovskite film

Figure 3 | (a) Overview of antisolvent timing, as indicated by the increase in perovskite XRD peak area induced by antisolvent addition . The time window for optimum antisolvent deposition is indicated in green. (b) Illustration of perovskite conversion routes for too late (top) and optimum (bottom) timing of antisolvent deposition.

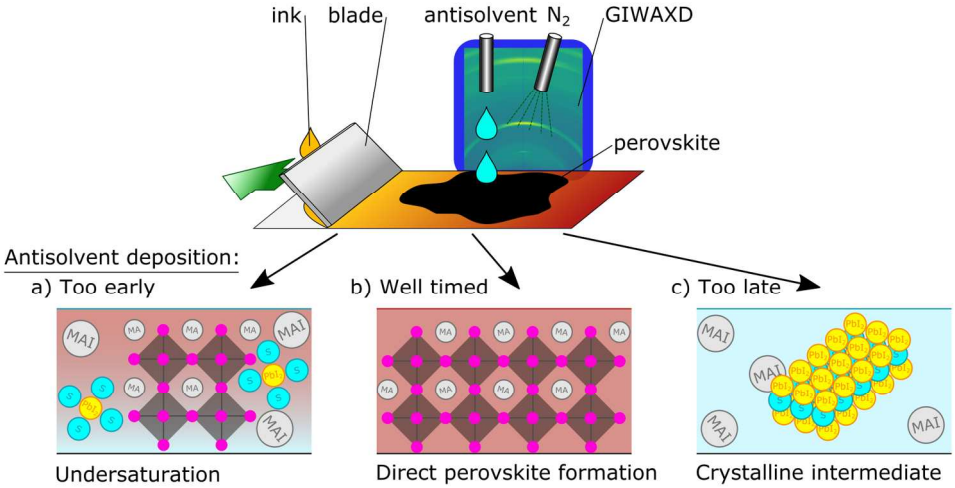
ink
blade
antisolvent N_2
GIWAXD
perovskite
Antisolvent deposition:
a) Too early
b) Well timed
c) Too late
Undersaturation
Direct perovskite formation
Crystalline intermediate